

FANCY MASTERARBEIT OF DEATH

Jonathan Förste

May 19, 2018

CONTENTS

1	INTRODUCTION	5
2	PHYSICAL PROPERTIES OF TRANSITION METAL DICHALCOGENIDE MONOLAYERS	7
2.1	Crystal structure and symmetries	7
2.2	Excitons in TMD monolayers	8
2.3	Spectral composition of wse ₂	8
2.3.1	Phonon sidebands	10
2.4	The valley zeeman effect	11
3	FABRICATION OF FIELD EFFECT STRUCTURES	13
3.1	Mechanical exfoliation	13
3.1.1	Layer number	14
3.2	Hexagonal boron nitride	14
3.3	Electrode fabrication	15
3.3.1	uv-lithography	16
3.3.2	Back gate electrodes	17
3.4	Hot pick-up and transfer	18
3.4.1	Annealing	20
3.5	Electrical characterization	20
4	SPECTROSCOPY OF WSe ₂ GATE DEVICES	23
4.1	Optical setup	23
4.2	Modelling peak shapes	25
4.3	WSe ₂ spectrum at different doping levels	27
4.3.1	Photoluminescence spectrum	27
4.3.2	Reflection spectrum	28
4.4	Measuring the valley zeeman effect	28
4.4.1	G-factors	29

1 INTRODUCTION

[1]

2 PHYSICAL PROPERTIES OF TRANSITION METAL DICHALCOGENIDE MONOLAYERS

2.1 CRYSTAL STRUCTURE AND SYMMETRIES

Like to all layered materials, TMDS consist of large covalently bound sheets, that are held together by the weak van-der-Waals force. And similar to graphite these sheets have a hexagonal lattice structure and form layers of only one unit-cell in the out-of-plane axis. It is the details of these unit-cells that distinguish TMDS from graphite and other layered materials. The fundamental building block of the bulk crystal is a single sheet – the monolayer – that consists of three atomic layers – A layer of transition metal atoms like tungsten (w) or molybdenum (Mo) sandwiched between two layers of chalcogen atoms like sulfur (s), selenium (se) or tellurium (t). This thesis is primarily concerned with tungsten-based TMDS: wse₂ and ws₂. TMDS can be in different phases, that have a different crystal structure as well as different electronic properties. The stable semiconducting phase is called 2H. In this configuration every transition-metal atom has six neighboring chalcogen atoms and forms a trigonal prismatic unit-cell, with the transition-metal in the center as depicted in figure 2.1 B. A TMD monolayer exhibits a D_{3h}^1 -symmetry. The unit-cell is invariant under 3-fold rotation as well as in-plane reflection. In the top-view (see figure 2.1 C) this looks similar to the hexagonal lattice structure of graphene, but with the key difference of a broken inversion symmetry. When the unit-cell is inverted with the transition metal atom as its inversion center, the chalcogen atoms wind up in empty locations as with any possible inversion point.

This has two important consequences, regarding the band structure. As in graphene, the reciprocal lattice is hexagonal. However at the edges of the Brilloin zone the degeneracy of the K-points is broken and instead of the characteristic Dirac cone of graphene, TMD monolayers form a direct band gap (see figure 2.2). The latter makes these materials very efficient photonic emitters, while the former enables so-called valley polarization. The local minima/maxima of the band structure (valleys) at the K and K' points can be selectively addressed with circularly polarized light of opposite helicity. The corresponding emission is of the same polarization as the incident beam. This effect demonstrates control over a new degree of freedom, the “valley index” and opened up the field of “valleytronics”, in which analogous to electronics and spintronics, the valley degree of freedom could be used by means of information processing[2, 3]. Additionally the valence band of TMDS, that is mostly composed of the d-orbitals of the heavy transition metal atoms exhibits strong spin-orbit coupling. The large splitting in the order of 150 meV couples the optical transition energy to the spin of the excited electron. Because this splitting is reversed in K' the valley-index is also coupled to the spin.

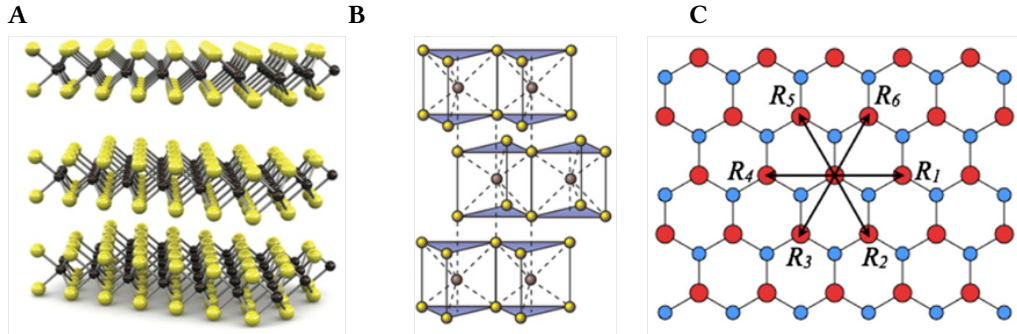


Figure 2.1: Crystal structure of TMDS: **A** TMDS are composed of large sheets of transition metal atoms sandwiched in between chalcogenite atoms. The covalent bonds strongly hold the layers together in-plane, while the individual sheets are only weakly bound by van-der-Waals forces. **B** In the 2H phase, the unit cell of TMDS has a triagonal prismatic shape with the transition metal in the center, between two triangles of chalcogenite atoms. **C** Viewed from the top, TMDS show a hexagonal lattice structure. However, because of the structure of the unit cell, the inversion symmetry is broken. Graphics from[2, 3]

2.2 EXCITONS IN TMD MONOLAYERS

What sets the light emission of TMDS apart from conventional direct band gap semiconductors is, that even at room temperature, the photoluminescence (PL) is dominated by the recombination of excitons. Excitons are bound pairs of an electron and a corresponding hole. In bulk semiconductors this bound state has a very low binding energy due to dielectric screening. The 2D-geometry of TMD monolayers however effectively reduces the screening effect, which results in strong Coulomb interaction between electron and hole. This raises the exciton binding energy to approximately 500 meV, which enables excitons to form well above room temperature[4]. The thinness of TMD monolayers has additional implications. Because the electric dipole field of the exciton extends beyond the boundaries of the crystal, the dielectric environment has a big influence on the optical spectrum[5–7]. Impurities such as microscopic water droplets or dangling bonds of silicon oxide can induce localized potentials, broadening the linewidth of the PL features, thus complicating spectroscopic studies. On the other hand, this high sensitivity could be used in quantum sensing applications to optically probe or visualize electric or magnetic proximity effects[8][referenz](#).

2.3 SPECTRAL COMPOSITION OF WSe₂

The optical spectrum of TMDS both in reflection and PL is dominated by excitonic effects. In wSe₂ especially the PL spectrum shows a rich ensemble of characteristic spectral features, that so far have not been identified completely and the discussion around the underlying processes is still active.

2.3 Spectral composition of WSe_2

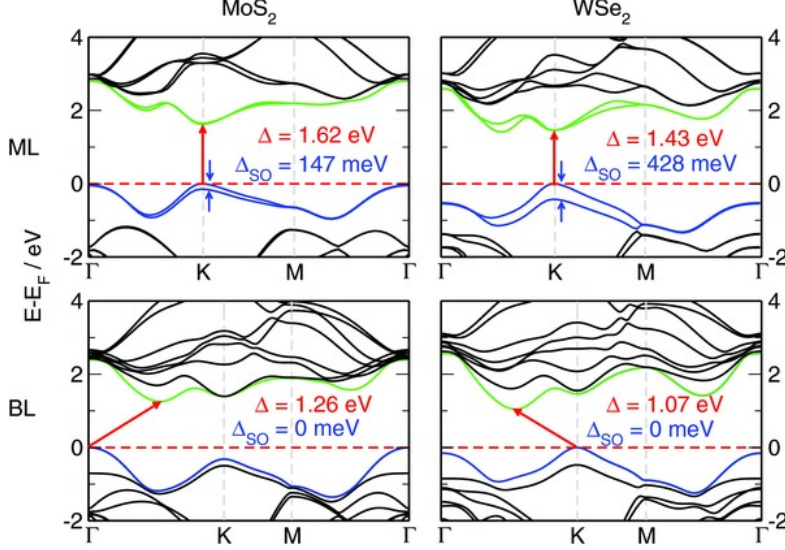


Figure 2.2: Band structure for MoS_2 and WSe_2 mono- and bilayers. In the limit of a single atomic layer TMDS form a direct band gap at the K -point and the valence band is strongly split due to spin-orbit coupling. Graphic taken from [9].

For hBN encapsulated WSe_2 the main exciton resonance (X) is located at around 1.72 eV. This resonance corresponds to the creation and annihilation of an exciton in the K valley with electron and hole having a parallel spin component (X_l). The corresponding exciton with antiparallel spins is often called the dark state as its “spin-forbidden” (D/X_u). Its radiative decay is only allowed in-plane, because of symmetry reasons™. Because of spin-orbit coupling this state lies about 40 meV lower than the bright exciton[10]. The PL from these excitons can be collected from the side or with a high numeric aperture objective, that catches light not directly emitted in the z -direction[11, 12]. In the presence of free charges, either holes or electrons, excitons can interact with them to form trions that are associated with a redshift of 20-30 meV[13]. While these properties can be predicted by modeling the trion as a three-body quasi particle, its precise nature still remains under discussion. The most contrarian interpretation to the helium-like bound state is a so-called fermi polaron. In a charged regime excitons behave like an impurity in a “sea” of electrons, forming the polaron quasi particle[14–16].

The spectrum of WSe_2 shows additional features, have so far escaped thorough understanding. In light of strong sample-to-sample variation, they are commonly attributed to localized effects, like defect-induced quantum dots or local doping[17, 18], that create trapped excitons. Improved fabrication techniques like mechanical exfoliation and the usage of hBN as a substrate (see section 3) have enabled experimentalists to measure spectra with very little defects and narrow linewidths, that still show a rich class of features, that are reproducible in other samples as well as in the samples used in this work.

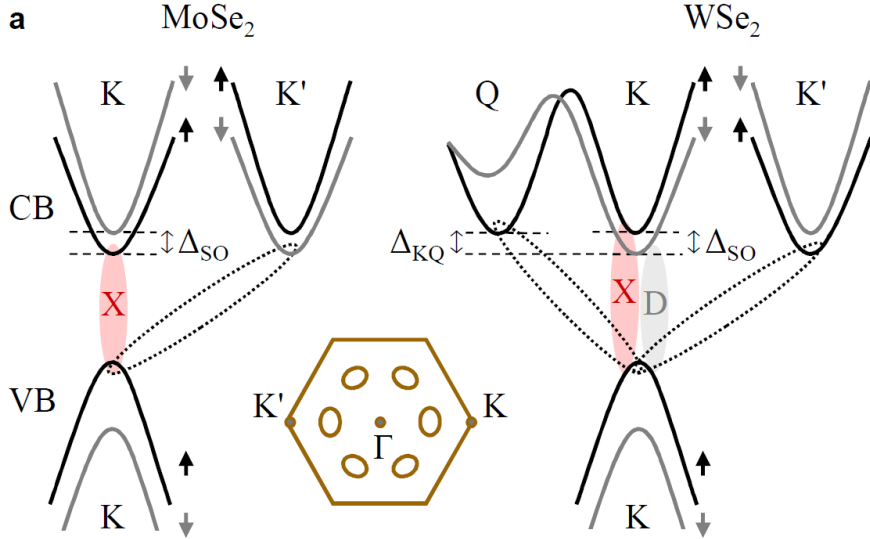


Figure 2.3

2.3.1 PHONON SIDEBANDS

Our group recently proposed a model identifying these peaks as phonon side-bands of momentum-indirect excitons[19]. It has recently been shown, that in contrast to molybdenum-based TMDS wse₂ actually shows an indirect band gap[20, 21]. As can be seen in figure 2.3, the Q-valley lies energetically close to the K-valley and is suggested to be lower than the upper K'-valley, that participates in the direct spin-like exciton transition. This could point to a high population of excitons composed of electrons in Q as well as in the lower lying spin-like K'-valley. While both these states are spin-allowed, momentum conservation prevents them from radiatively decaying in a single-photon process. Instead they can recombine with assistance of an additional phonon, carrying the inter-valley momentum. For momentum conservation to hold the following equations has to be fulfilled for momentum-indirect excitons in Q or K' respectively:

$$\vec{k}_K + (\vec{k}_K - \vec{k}_{Q/K'}) = \vec{k}_K + \vec{k}_\gamma + \vec{k}_{phonon} \quad (2.1)$$

$$\Rightarrow \vec{k}_{phonon} \stackrel{!}{=} \vec{k}_K - \vec{k}_{Q/K'} \quad (2.2)$$

Because of the hexagonal structure of the Brillouin zone $\vec{k}_K - \vec{k}_{K'}$ simply equals a phonon in K whilst $\vec{k}_K - \vec{k}_Q$ is conveniently close to a phonon in Q. Crystal vibrations in TMDS can have three acoustic and six optical modes, but only two acoustic and three optical modes can couple to charge carriers. This leaves a total of five possible phonon sidebands for both Q- and K'-indirect excitons, neglecting processes involving more than one phonon. Corresponding, theoretically calculated energies can be found in 2.4[22]. The phonon replica would appear as a peak redshifted by these energy values. For K'-indirect excitons the positions of the peaks can be inferred directly, since the energy splitting between the spin-like and spin-unlike exciton is known and both features can be measured. The Q-valley however has no direct decay channel.

Mode	K	Q
TA	15.6	11.6
LA	18.0	14.3
TO(E')	26.7	27.3
LO(E')	31.5	32.5
A ₁	31.0	30.4

Figure 2.4: [22]

Its energy thus has to be fixed inductively, by looking for peaks that fit the pattern, given by the phonon energies and calculate backwards.

[23]

2.4 THE VALLEY ZEEMAN EFFECT

A splitting of spectral lines in presence of a magnetic field has been studied for over a hundred years and is called the Zeeman effect, named after the scientist first measuring it in the spectral lines of sodium. The shift of different energy levels in an atom results from the magnetic moment of the state, caused by its orbital angular momentum and spin. Solid crystals are essentially large ensembles of atoms that merge atomic orbitals to form the electronic band structure, that can shift in a magnetic field just as orbitals of single atoms. The 2D-nature of TMD monolayers and their broken degeneracy of the K and K' point gives rise to a meta-phenomenon called the “valley Zeeman effect”, that leads to a shift in the band gap energy that is different for both valleys, leading to a split of spectral lines with different circular polarization[24]. In the vicinity of the K point the band structure is dominated by the large d-orbitals of the transition metal atoms. The hybridized $d_{x^2-y^2} \pm id_{xy}$ orbitals carry orbital angular momentum and a magnetic dipole moment. The TMD-geometry confines electron movement to the 2D plane, forcing the magnetic moment to either point upwards or downwards out of plane. This direction is exactly opposite at the K and K' points, shifting the valence band energy, and thus the band-gap in opposite directions. For the direct exciton transition the observed magnetic moment has a value of $\pm 2\mu_B$, leading to a valley splitting of $\Delta_{K,K'}=4\mu_B B$. The prefactor in this equation is often called the g-factor and is given in units of the Bohr magneton $\mu_B=e\hbar/2m_e$.

The precise prediction of the g-factor for different states is a nontrivial task as predicting the shift in the band structure requires knowledge of the quasi particle effective mass and has to take into account the spin of the excitons components and its magnetic moment, that is governed by the strong coulomb exchange interaction. [25]

3 FABRICATION OF FIELD EFFECT STRUCTURES

The fabrication of a functioning field effect structure of TMD mono- or bilayers roughly consists of three different procedures. The production of suitable flakes of TMD's, the preparation of an electrode both on the sample and in the substrate and the assembly of the full device on top of it.

3.1 MECHANICAL EXFOLIATION

Thin films of TMDS, like many natomaterials, can be fabricated using a top-down or bottom-up approach. The bottom-up approach for these particular materials is called chemical-vapor deposition (cvd)[26]. Because of its scalability it is the leading candidate that could be used in an industrial fabrication pipeline. However, the top-down approach of mechanical exfoliation has become the first choice for a lot of projects to build high quality model systems, that can be used to study physics in low dimensions[27]. The reason is the so far superior quality of few-layer flakes in terms of defects and contaminants as well as the synergy with dry transfer methods(Reference(Laterchapter)).

The mechanical exfoliation process – often referred to as the “scotch tape method” – is based on the fact, that the van-der-Waals forces between adjacent layers in TMD's are much weaker, than the lateral covalent bonds inside them. In fact, they are weak enough, that they can be easily broken apart by adhesive tape. The starting point is a solid crystal of TMD-material, that can be produced either naturally or synthetically with high purity (supplied by hq-graphene). When a stripe of adhesive tape is brought in contact with it, a small amount can be peeled off. With a second stripe, that is put on the first one, the process is repeated multiple times. Each time, the fresh tape is peeled of its parent, the strong adhesion between tape and TMD ensures a clean interface. Three to four repetitions are an optimum to produce monolayers of a useful size. More repetitions further thin the material but heighten the risk of these thin films to break to smaller pieces, which complicates processing the flakes later on and build larger devices.

To prepare monolayer flakes for the assembly of more complex devices, they first have to be transferred onto a suitable substrate. In this work, this substrate is silicon with a layer of thermal oxide that is between 50 and 90 nm thick. Before wafers of this material are brought in contact with the exfoliation tapes they are cleaned both in acetone and isopropanole before being exposed to oxygen plasma for 180 s. This ensures a clean surface and maximizes the material that sticks to the wafer(Reference). After the tape is in contact, the wafer is heated to 90°C. After cooling down the tape can be peeled off and the wafer is inspected for monolayers. As seen in [Figure], during this process a large number of flakes of different sizes and thicknesses are transferred and it is uncommon to find more than one monolayer of suitable size on a wafer of 10 by 10 mm.

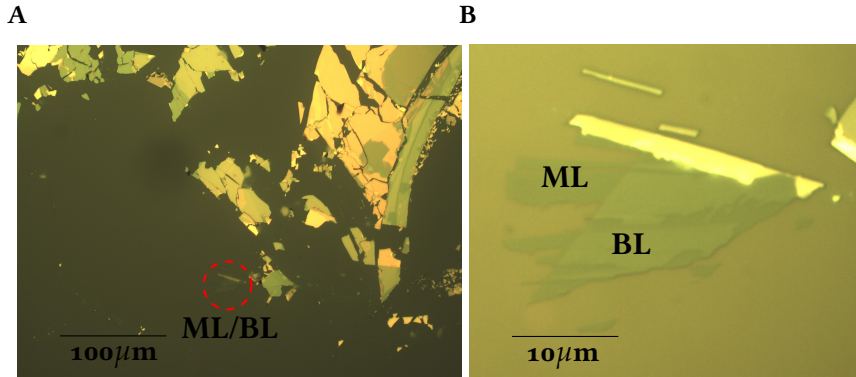


Figure 3.1: **A** During the exfoliation process a lot of flakes of different size and thickness are scattered over the substrate. Interesting specimen have to be searched for by hand. **B** Flake consting of mono- and bilayer regions that can be identified by their optical contrast.

3.1.1 LAYER NUMBER

Under an optical microscope monolayers can be identified using the optical contrast and the color. It is possible to verify the layer number by this criteria alone using a camera and image analysis software[28], however this is much more reliable on transparent substrates, since the optical contrast is higher and the lighting conditions can be controlled more precisely. With our optical microscope and si/sio₂ substrates, monolayer candidates where instead verified using photoluminescence (PL) imaging(Referenz Andre). Because of the direct band-gap, monolayers of TMD's are much more efficient emitters than even bilayers with almost an order of magnitude difference in PL-intesity. The result can be seen in Figure 3.2. The sample is excited with a laser with a wavelength above the A-exciton resonance and only the PL is collected on the chip of a USB-camera. A detailed description of the optical setup can be found in (Optical Setup). As can be seen, the PL-image clearly identifies the monolayer-regions through bright intensity, while the bilayer region of the flake is not visible at all. On the microscope picture on the other hand, both regions do not differ much in color and reflectance and can be tricky to tell appart, especially when the lighting is inhomogenous or changes over time.

Other methods to idetify monolayers inclcude both photoluminescence and Raman spectroscopy[29–31]. However, for assembling devices and verifying the quality of exfoliated flakes, PL-imaging proved to be the fastest and most versatile method.

3.2 HEXAGONAL BORON NITRIDE

For spectroscopic studies of TMD's the right substrate plays a very crucial parts. As discussed in section 2.2, the ultrathin geometry of TMD monolayers makes them very sensitive to the dielectric environment. To obtain a narrow linewidth of the spectral features both in reflection and PL spectroscopy, a suitable substrate not only has to have a minimal roughness on the

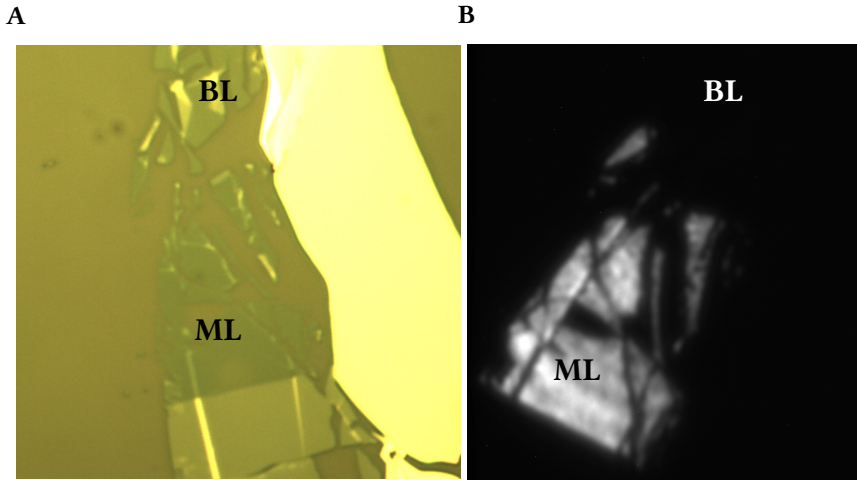


Figure 3.2: Comparison of mono- and bilayers of WSe_2 . **A** The reflectance contrast of mono- and bilayers can be used to measure the layer number. The difference is however small enough to misidentify them under changing or inhomogenous lighting conditions. **B** The monolayer shows much higher PL-intensity than the bilayer and can therefore be identified very easily.

surface that should ideally be atomically flat, to avoid modulation of the band structure through strain. Also, the substrate has to be dielectrically calm to avoid perturbation of excitons by dangling bonds, that reduce lifetimes and broaden the spectral lines. Both criteria rule out traditional substrates such as Si and SiO_2 . In recent years hexagonal boron nitride (hBN) has proven to be the superior choice to observe narrow linewidth spectra in TMD's[32]. hBN, just like TMDS is a layered material, but belongs to the class of 2D-isolators, with a large, indirect band gap in the uv-range[33]. Thin, flat layers of hBN can be mechanically exfoliated and can achieve large, flat terraces. Few layers are sufficient to shield a TMD sample from the underlying substrate. To achieve even narrower lines, it can be "sandwiched" between two flakes of flat hBN as was done with all samples contributing to this thesis. From the standpoint of nanofabrication hBN has another important property. The van-der-Waals forces at hBN-TMD interfaces are stronger than between a TMD sample and SiO_2 . This enables the hot pick up assembly, discussed in section 3.4.

3.3 ELECTRODE FABRICATION

The goal of this thesis was, to fabricate high quality TMD-monolayer samples that are gate-tunable, meaning control over the charge density inside the monolayer flake leveraging the field effect. The problem of designing such a device can be understood as using the 2D-material as one plate of a capacitor, and charging it, by applying a voltage. The other plate or "back-gate" in this analogy is the conducting boron-doped silicon substrate. Flake and substrate are separated by a 50nm layer of thermal silicon-dioxide, that functions as the dielectric of the

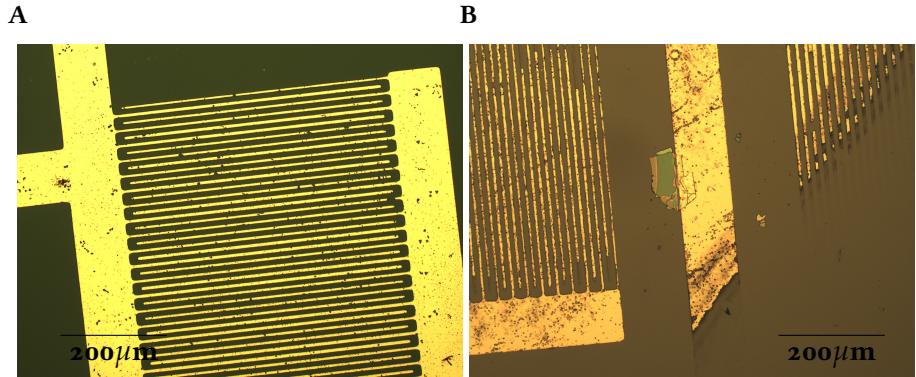


Figure 3.3: **A** Electrodes are written onto the substrate prior to the assembly of the hBN-TMD heterostructure. A preused chromium mask of an interdigital structure is used for the gold pattern. **B** As long the heterostructure is dropped in contact with a thick line of the gold pattern, minor defects in the electrode structure do not affect the functionality of the device.

gate-structure. Both the sample on top and the back-gate have to be contacted to allow the application of a voltage.

3.3.1 UV-LITHOGRAPHY

In many gated devices, that incorporate TMD-monolayers, the gate electrodes are actually fabricated directly onto the sample as a last step(Referenzen). While the fabrication of contacts can be more precisely tailored in this way, the big drawback is the exposure of the monolayers to a lot of chemicals like photoresist and developer, that can contaminate the sample and lower its quality. Therefore in this work a more simple approach was chosen. Instead of writing contacts after transfer, contacts are fabricated beforehand. The encapsulated hBN-TMD-heterostructure can be contacted by dropping it on the edge of the gold structure. The gold patterns are created using contact lithography using a chromium mask, deposited on glass. Because the heterostructure can be dropped at any point on the substrate, the precise shape of the gold structure is unimportant. Therefore no new lithographic mask had to be fabricated. Instead a suitable mask was chosen from old preused structures. The downside is, that these masks can deteriorate over time and over many uses, but because of the low requirements for the electrodes all its defects manifest themselves in a purely aesthetic manner and do not affect its functionality. The process starts with spin coating AZ701-photoresist on a si/sio₂ wafer. Using the blabla-Maskaligner, the wafer is brought in contact with the mask before exposing it to uv-light for 18 seconds. After that, the pattern is developed using blabla-developer, that washes out the exposed photoresist.

In the next step, the sample is coated in an X-ray evaporation system. First, a 1-5nm film of titanium is deposited on the substrate, that acts as a bonding agent. Subsequently a 50nm film of gold is deposited ontop, that forms the actual top-gate electrode. After removing the sample from the high-vacuum chamber the undeveloped photoresist is removed in the so

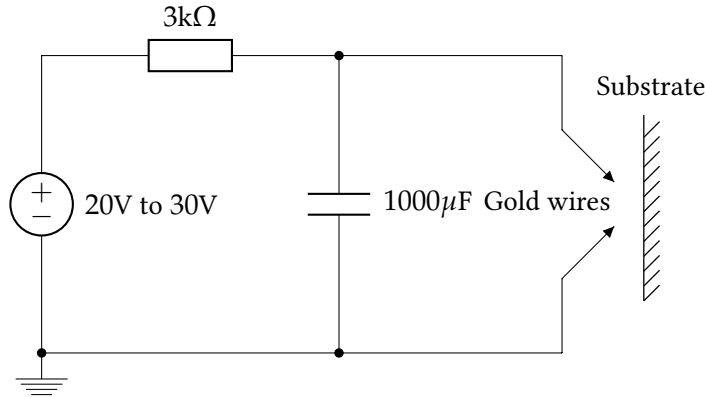


Figure 3.4: Circuit diagram for back gate fabrication: A capacitor is charged at 20V to 30V. Two boron-doped gold wires are moved very closely to the silicon substrates. Once the distance between the wires and the substrate is low enough, an electric arc will form, when the capacitor discharges through the substrate. The heat from the current liquifies the tip of the gold wire, which diffuses inside the silicon and “smears out” the semiconductor/metal-interface.

called “lift-off”. The substrate is simply bathed in acetone, that desolves the resist below most of the deposited gold and only the structures in the developed areas remain. To speed up the lift-off process, the sample can be placed in an ultrasonic cleaner at a low power. The resulting structure can be seen in Figure 3.3.

3.3.2 BACK GATE ELECTRODES

Silicon is a semiconductor. A simple contact with a metal wire therefore results in a Schottky barrier at low temperatures even with a moderately doped substrate like the ones used in this thesis. To create an ohmic contact, to the backgate, the semiconductor/metal interface is “smeared out” by diffusing boron doped gold into the substrate. This is achieved by applying a voltage (20 V to 30 V) between two gold wires and bringing them close to the substrate. Because the substrate has a higher conductivity than the ambient air, an arc discharge between the tips of the wires will preferably find its way through the substrate. When the arc forms upon bringing the wires very close to the substrate and each other the ohmic heat will liquify the tips of the wires and inject gold into the topmost layers of the silicon. This creates a gradual metal-semiconductor interface and avoids a Schottky barrier.

This process can be very violent. Gold droplets can splash over a large distance and gold can not only diffuse into the backgate but can also contaminate the SiO_2 dielectric, lowering the breakdown voltage significantly. Therefore this step in the fabrication process should be taken before assembling the TMD-hBN heterostructure. This way, the substrate can be replaced in case of failure.

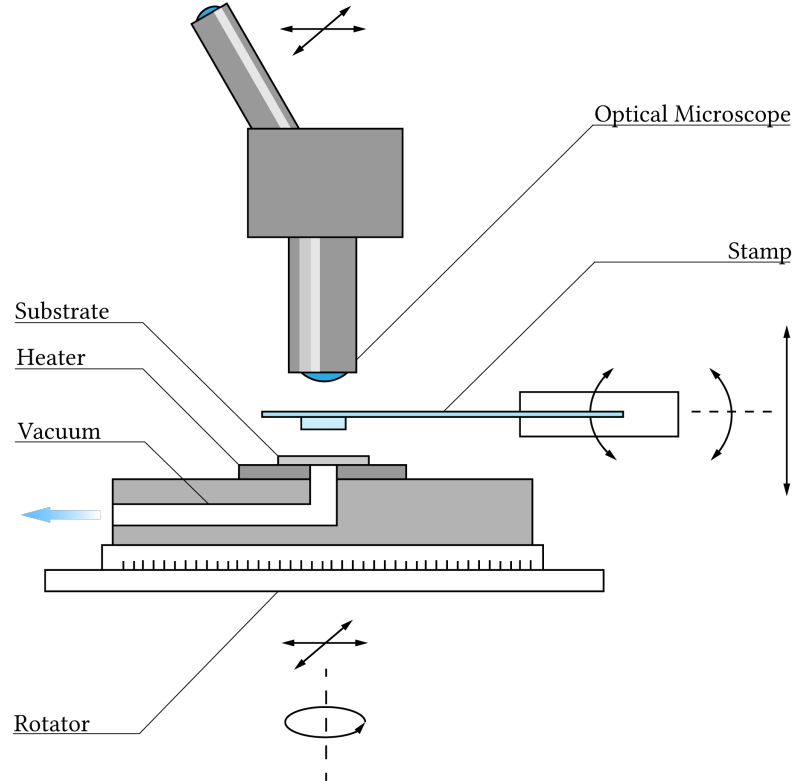


Figure 3.5: Setup for hot pick-up and stamping. The substrate is placed on a small, round **ceramic heater** with a 3mm hole in the center(Referenz Thorlabs), that is PID-controlled and can reach temperatures up to 200°C. It is mounted airtight onto the massive sample holder, that is connected to a **vacuum pump** to hold the **substrate** in place. It is **fully rotatable** and can be moved in plane. The **PDMS/PPC stamp** is monted to a z-translator and can be tilted with respects to both in-plane axes. The **optical microscope** can also be moved in-plane.

3.4 HOT PICK-UP AND TRANSFER

The mechanical exfoliation method is popular also for its synergy with dry transfer methods. CVD-grown TMD-flakes are grown on suitable substrates and can be transferred to target substrate using a variation of wet methods, that involve powerful solvents or a combination of solvents and polymer films to lift the grown flakes off their initial substrate [34]. The advantage of the exfoliation method in this regard is that flakes can be put on any substrate directly from the adhesive tape. That led to the invention of “viscoelastic stamping”, where the TMD-material is exfoliated on a substrate of viscoelastic polymer called polydimethylsiloxane (PDMS)[35]. This so called “stamp” could then be brought in contact with the target substrate and peeled off carefully to drop down the flake at a desired position, opening up the possibility of producing carefully designed heterostructures deterministically.

The use of hBN to provide an optimal dielectric environment opened up the possibility of

using the van-der-Walls forces between hBN and 2D-materials not only to drop down exfoliated layers, flake by flake but to pick up 2D-materials with hBN-flakes, increasing the yield as well as ensuring very clean interfaces, free of contaminants from the polymer stamp.

The method used for this work is called “hot pick-up and stamping”[36, 37]. The stamp used in this process is a block of PDMS, mounted on a glass slide with transparent adhesive tape. This block is spin-coated with a polymer polypropylene carbonate (PPC). To make sure, that the polar PPC sticks to the stamp while being heated to high temperatures it is treated in oxygen plasma for at least 20 minutes before spin coating[38].

The TMD-flake is exfoliated on a Si/SiO₂ substrate and so are suitable bottom and top hBN flakes. The primary criteria for finding the right hBN-flakes is the flatness of its surface, so that the TMD-flake can be encapsulated between two large terraces without cracks or steps. To allow a fast fabrication process, this flatness is only judged with help of an optical microscope. More sophisticated methods like atomic force microscopy can be used to verify the flatness more accurately, however this not only extends the fabrication process but does not help determining the quality of the top hBN-flake, since its interface is facing down after being exfoliated on the parent substrate.

The goal of the hot pick-up is now to use a hot-plate to control the van-der-Waals forces between hBN, TMDs and the substrate to ensure adhesion between the parts of the heterostructure as well as to reduce contamination with water molecules from the ambient air.

After all precursors are prepared on Si/SiO₂ substrates, the actual pick-up and stamping process can be carried out. The fabrication setup can be seen in (Figure whatever). The first step is the pick-up of the top hBN flake. At 40°C the van-der-Waals forces between hBN and PPC are already strong enough to lift the flake off the silicon substrate. In the next step the hBN is dropped on the TMD-flake. To make the interface as clean as possible the temperature for this drop is raised to 110°C. This ensures a stronger van-der-Waals force between hBN and TMD than between TMD and silicon-dioxide but more importantly contamination through droplets of water from the ambient air is minimized above its boiling point and other contaminants are more mobile as well. By slowly pressing the stamp against the substrate, this dirt can leave the interface of the two flakes and fewer blisters form(hotpickuppaper). The stack of TMD and hBN can then be picked up again following the same procedure that was used for the bare hBN flake. Afterwards it is dropped down on the bottom hBN flake. To contact the TMD flake to gold part of it has to remain outside the hBN encapsulation. This part does not necessarily have to be a monolayer but can also be any form of TMD, that is in contact with it so charges can be transported. The hBN on the other hand is elastic enough so that thicker material does not affect the encapsulation of mono- or bilayer regions.

The last step is to transfer the whole stack to its final position in contact with the electrodes. This is accomplished by repeating the pick-up process once again and dropping the stack in contact with the gold structure.

Despite the strong plasma treatment of the PDMS-stamp in some cases the PPC can peel off during the drop down part of the transfer due to high heat as the polymer becomes ever more liquid. In this case the sample can be carefully treated with acetone, which dissolves the polymer rapidly. The sample subsequently has to be cleaned in isopropanol and blown dry with nitrogen gas.

3.4.1 ANNEALING

While the hot pick-up should in theory ensure a hBN-TMD interface free of contamination, especially contamination due to humidity in the ambient air can remain between the layers and seriously lower the quality of the sample. To remove this pollution, the sample can be annealed[39]. During annealing, the sample is placed in an annealing oven. While maintaining a high vacuum of 10^{-3} mbar, the oven heats the sample to 250°C for three hours. Other recipes, that use higher or lower temperatures or longer annealing times can work just as well. Since the hot pick-up technique should keep the TMD surfaces clean of anything but the ambient air, the only concern is water, which is removed more easily than other contaminants. More aggressive recipes, that work at higher temperatures or for longer times to remove also polymer contaminations that arise from contact to the stamp and therefore have a limited advantage over milder annealing conditions, but raise the risk of damaging the sample through temperature induced strain, that can potentially rip the TMD flakes.

3.5 ELECTRICAL CHARACTERIZATION

To assess the quality of the the gate structure, its breakdown voltage has to be determined. This is the voltage between top gate and back gate, at which the leakage current starts to rise exponentially by forming conducting channels through the dielectric, that are self-sustaining and lift the conductance permanently[40]. This breakdown voltage complicated to predict, as it is a nonlinear effect mainly caused by faults in the SiO_2 layer. Thus it does not only depend on the thickness of the dielectric but also on the area of the top gate, because the statistical chance of a conducting channel forming is higher the more area of the sample is covered with conducting material. Additionally the rather violent ohmic contacting of the backgate can also damage the dielectric and lower the breakdown voltage. Therefore each sample has to be classified before being used to tune the charge density in spectroscopy. The dielectric in samples used throughout this thesis had a thickness of 50 nm or 90 nm, corresponding through a predicted breakdown voltage of 47.5 V or 85.5 V respectively. To assert these values, the leakage currents have to be monitored while ramping up the voltage. Before breakdown these currents are of the order of 100 pA to 1 nA and can be measured using a lock-in amplifier. A constant voltage across the desired range of operation ($\pm 30\text{V}$) is added to a small AC-voltage of small amplitude ($U_0 = 10 \text{ mV}_{pp}, f = 77.1 \text{ Hz}$). A diagram of the circuitry is drawn in figure 3.6. The real part of the resulting current is the resistive current, or leakage and the imaginary part is proportional to the capacity. Both parts can be measured and monitored in the lock-in amplifier. The DC-voltage is ramped until the leakage rises exponentially. At this point, the currents are still small enough to not inflict permanent damage to the dielectric and give the safe range of positive ad negative voltages during operation during the experiment.

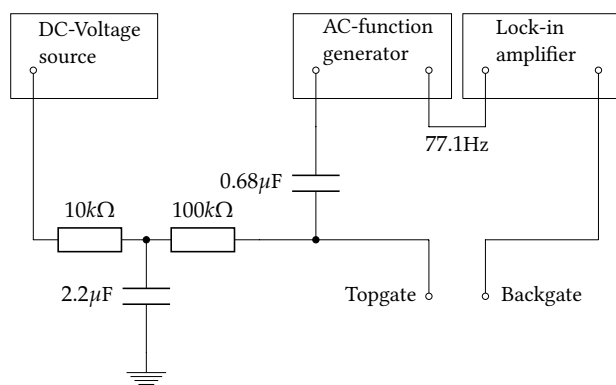


Figure 3.6: Diagram for the cv-measurement. Using a lock-in amplifier and a small AC voltage even very small resistive currents leaking through the samples dielectric can be measured. This way, the maximum DC voltage at the gate can be obtained, by ramping a DC voltage source until the resistive current starts to rise exponentially.

4 SPECTROSCOPY OF WSe₂ GATE DEVICES

The goal of this thesis was to advance tools that can help understanding the optical spectra of TMD monolayers. In this chapter the experimental tools and results will be discussed in more detail. The narrow linewidth of the spectral features due to hBN encapsulation enables the possibility of analyzing the lines of the optical spectrum individually. This is accomplished by tracking their position and shape though different charge densities and magnetic field strengths. The measurements, discussed in the coming chapter are all performed on a sample of tungsten-diselenide (WSe₂). Tungsten-based TMDS are of particular interest, because their complex band-structure yields a rich spectrum, that is still poorly understood.

4.1 OPTICAL SETUP

The optical setup is a confocal microscope. This means that the sample is placed in the focal plane of a low temperature objective and instead of capturing a wide field image of the sample only the signal from the focal point is collected. The advantage is a high spatial resolution as well as a superior ratio between excitation power and collected signal, which is an important factor for spectroscopy as signal to noise ratio as well as integration time are critical factors in an experiment in which many spectra have to be recorded. A diagram of the complete setup can be seen in figure 4.1. The excitation beam from a laser is guided to the so called excitation arm with a single mode optical fibre. It passes though a linear polarizer to define a polarization axis and is reflected to the objective by a beam-sampler. To analyze circular dichroism in the detected beam, it passes through a quarter waveplate and another linear polarizer before being coupled into another optical fibre, that is connected to a spectrometer. The sample is mounted on a piezo nanopositioner inside a cryostat or container of liquid helium and connected to a voltage source, to tune the charge density in the TMD flake. A strong, homogenous magnetic field along the z-axis of the sample can be supplied by a superconducting magnet.

For PL spectroscopy, the sample is excited by a laser beam with a narrow frequency profile and high power. Because this beam has a much higher intensity, than the collected PL it is tuned to a higher frequency than the main exciton resonance, to obtain a complete spectrum without features from the excitation beam. To avoid stray light inside the spectrometer a longpass filter additionally blocks the laser before entering the detection fiber. A shortpass filter in the excitation arm blocks Raman modes of the optical fiber, a result from high excitation power, that can have frequencies overlapping with the PL of the sample. When the setup is operated for reflection spectroscopy these filters are omitted. Instead, the sample is illuminated with a broad band white light source at a low power. To find the signal, a background spectrum, recorded in absence of the TMD flake is substracted from the main spectrum.

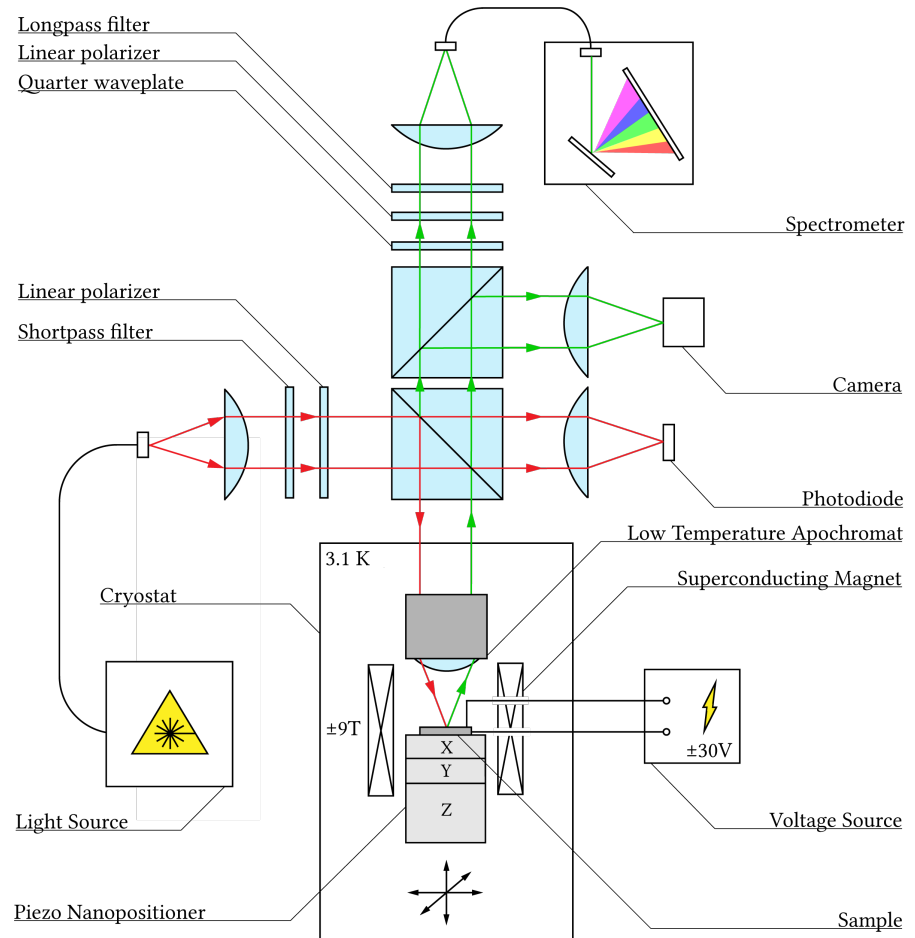


Figure 4.1: Optical setup for confocal spectroscopy: Light from a **laser**-source is guided to the setup in a single mode optical fibre and collimated. To cut off raman-modes, that are created in the fibre a **shortpass** filter is installed behind the collimator. A **linear polarizer** defines a polarization axis. A **beam-sampler** is reflecting the excitation beam into a **low temperature apochromat**, whose focus lies on the sample, with a spotsize of $\sim 0.5\mu\text{m}$. The sample is mounted on a **piezo nanopositioner**, that is placed inside a **cryostat** at a temperature of up to 3.1 K or in a container of liquid helium at 4.2 K . The cryostat is equipped with a **superconducting magnet** that can supply a homogenous magnetic field up to 9 T . The sample electrodes are connected to a **voltage source** (Yokogawa) that supplies $\pm 32\text{ V}$. The detection spot is identical with the excitation. The reflection or photoluminescence is collimated again in the objective and passes through a σ^-/σ^+ -analyzer consisting of a **quarter waveplate** and a **linear polarizer**, before being focussed in the detection fibre that connects to a **spectrometer**. A **camera** can be used to monitor the spot and image the sample, if it is brought out of focus.

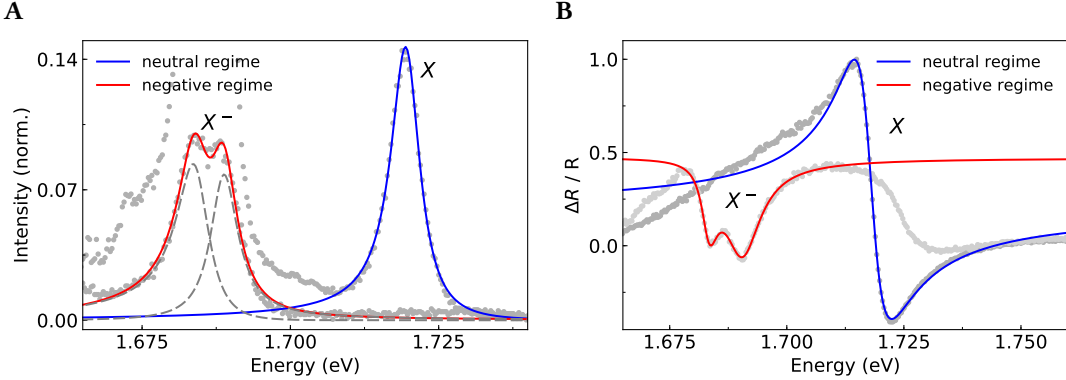


Figure 4.2: Fits of the exciton (X) and trion (X^-) features in a neutral and negatively charged spectrum. **A PL**: The lineshape in the fitting model is a lorentzian with adaptive linewidth to model the slight asymmetry of the peaks. It is tuned with a sigmoid function, according to a symmetry parameter. The double-peak of the trion feature is a sum of two asymmetric lorentzians. **B Reflection**: The exciton resonance in this hBN encapsulated sample does not show a clean dip and can be approximated by a model function corresponding to the scattering cross section of a fano resonance. The trion double dip can be fitted using a sum of two asymmetric lorentzians. However, in contrast to the PL fit, a constant shifting parameter is added, and the starting values for the scaling parameter are chosen negative.

$$S_R = \frac{\Delta R}{R} = \frac{R_{\text{flake}} - R_{\text{background}}}{R_{\text{background}}} \quad (4.1)$$

The signal S_R is the difference of the Reflection signals of TMD flake and background. The division by the background reflection is made to normalize the signal. The resulting reflection spectrum should show only features, of the flake. In practice, the obtained data has to be evaluated with some precautions in mind, to avoid misidentifying for example interference effects due to differences in hBN thickness as features of the absorption behavior of the sample.

4.2 MODELLING PEAK SHAPES

To precisely quantify positions and linewidths of the spectral features, they have to be modelled using appropriate fitting functions. In PL all peaks should ideally have a lorentzian line shape (see Figure 4.3 A).

$$i(\nu) = \frac{a}{1 + \epsilon^2} \quad (4.2)$$

$$\epsilon = \frac{\nu_0 - \nu}{\gamma/2} \quad (4.3)$$

where I is the intensity, ϵ is the reduced energy, composed of the energy ν , the peak position ν_0 the linewidth γ at FWHM. For a maximum value a of 1, the function is normalized. In the

crowded spectrum of an imperfect sample however, this is only an approximation, as the different peaks blend together and can have fine structures, that cannot be resolved as individual features. This leads not only to a broadening of the lines, but also skews the line shape, mostly resulting in a “red shoulder” – higher intensity towards the low-energy end of the peak. To accurately model these features and get good estimates for peak positions as well as linewidths the lorentzian has to be expanded. A generic way of modelling an asymmetric line, that is close to the “natural” linewidth is using a lorentzian with variable linewidth γ , meaning the static linewidth of in 4.3 is replaced by a smooth sigmoid function, that includes an additional symmetry parameter[41].

$$\gamma = \frac{2\gamma_0}{1 + e^{k(\nu - \nu_0)}} \quad (4.4)$$

This value is then inserted into (4.3). The symmetry parameter k scales the steepness of the sigmoid function and thus the skewedness of the lineshape. The γ_0 parameter is identical to γ at ν_0 and corresponds to the peaks linewidth. For $k = 0$ (4.3) collapses to γ_0 and the standard lorentz lineshape is recovered. The asymmetric lorentzian can be used to model all peaks in the PL spectrum.

In reflection spectroscopy, the signal should correspond to the absorption of the sample. Therefore the straight forward way to model features would base on a lorentzian function as well, only with a negative sign¹. However, in an hBN-encapsulated sample, the spectrum can be more complicated (see Figure 4.4). The trion signal in the charged spectrum shows a double dip. This can be modelled by simply adding two negative asymmetric lorentzians and compensating for the positive offset with an additional constant parameter simply added to the function. The main exciton resonance however has a highly asymmetric lineshape, that cannot be modeled with a bare lorentzian (either (4.3) or (4.4)). A more general function is a so called fano resonace. The physical background is the interference between a resonance and a continuous background[42]. In case of encapsulated TMD monolayers, this lineshape stems from interference effects of the hBN substrate[43].

$$\frac{(q + \epsilon)^2}{(1 + \epsilon^2)} = 1 + \frac{q^2 + 2q\epsilon - 1}{1 + \epsilon^2} \quad (4.5)$$

where q is the so-called fano parameter. This can be seen as a more general form of (4.3). For $q = 0$ the shape of (4.5) reduces to a downwards facing lorentzian. Just like for the trion and all PL features, the linewidth parameter for (4.4) can be deployed to skew the function to better fit real data. Examples of the fitting process for reflection and PL spectra can be seen in figure 4.2. To use the explained fitting functions, the data was sliced to isolate and fit each feature.

Besides quantifying the sample quality via the linewidth parameter, the described fitting procedures were extensively used in the next section to find peak positions at different doping levels and different magnetic fields.

¹The sign of the fitting functions depends on the definition of the spectrum itself. In this work, the background is subtracted from the signal, yielding the reflection off the flake. A flipped sign on the other hand corresponds to the absorption.

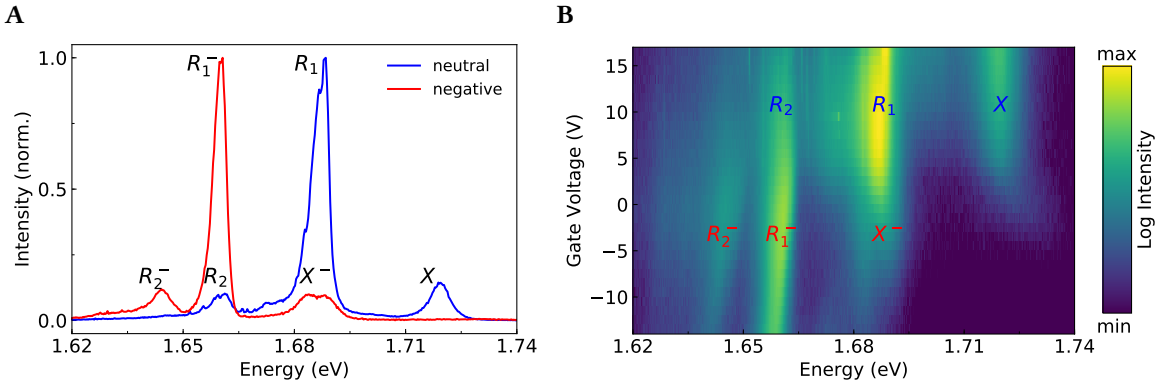


Figure 4.3: Photoluminescence of wSe₂ at different doping levels. **A** Spectra in the neutral and negatively charged regime. The PL of the exciton (X) is clearly visible at the blue end of the spectrum. The replica peaks (R_1 , R_2) correspond to acoustic phonon sidebands of Q- and K'-indirect excitons with low-intensity features to the red indicating optical sidebands. In a negatively charged regime, they vanish in favor of redshifted peaks, that correspond to the trion (X^-) that is split by electron-electron exchange interaction, and its momentum indirect counterparts. While R_1^- fits the picture as an acoustic sideband of X^- , R_2^- seems to be the charged spin-unlike dark state. **B** Spectral features in a gate-sweep. The plot can be divided into a neutral and charged regime below and above 5V. This threshold is a signature of unintentional n-doping and varies across the sample.

4.3 WSe₂ SPECTRUM AT DIFFERENT DOPING LEVELS

The general composition of the wSe₂ spectrum was described in 2.3. With a functioning gate-tunable sample with narrow linewidths these features can be explored and individually studied.

4.3.1 PHOTOLUMINESCENCE SPECTRUM

The PL spectrum is pictured in figure 4.3 both in a neutral and charged regime. Exfoliated TMDS are often unintentionally doped negatively (Referenz). Therefore the positive regime could not be probed in this sample. The peak to the blue end of the spectrum belongs direct spin-like exciton (X). This peak is well understood and can therefore be used to benchmark the spectral linewidth and the overall quality of the sample. With a linewidth of 6.8 meV the exciton is still above the intrinsic homogeneous linewidth which is reported to be below 2 meV[44, 45]. Inhomogeneous broadening can be mostly attributed to local changes in the potential landscape that can arise from defects, impurities as well as strain induced shifts in the band structure[46]. The diffraction limited spot of the objective is large enough to cover a large ensemble of slightly different contributions to the PL signal, that merge to a broad peak. Apart from the FWHM linewidth of the exciton peak, both a significant asymmetry parameter in the fit as well as a slight deviation from the lorentzian line-shape are indicators, that the feature has an considerable substructure and there is still room for improvement in terms of

sample fabrication.

However, the linewidth-limited resolution of the present sample is good enough to distinguish the fine splitting of the trion peak in the charged regime (X^-). When the gate voltage is tuned, the Fermi level is shifted. The negative regime is reached when the Fermi level rises above the lower K and K' valleys in the conduction band and free charge carriers enter the flake. Optically excited excitons can bind electrons from either of the two valleys resulting in two a-priori degenerate trion states, that differ energetically because of a difference in Coulomb exchange interaction [13]. The resulting splitting can be resolved in the present sample and has a value of 5.2 meV. The spectral difference to the exciton peak in the neutral regime gives an estimate of an additional trion binding energy. Taking into account the exchange splitting it has a value of 30.5 - 35.8 meV. Since the separation of the two trion peaks is quite low, the linewidth estimates from the fit are only a rough estimate but are close to the neutral exciton at 5-7 meV showing the close relation of both features.

The peaks to the red in both the neutral and charged spectra can be explained using the phonon sideband model described in 2.3.1. The Q -indirect exciton should lie above the direct spin-unlike state. Therefore it makes sense to identify the intense R_1 peak with its acoustic sidebands, putting the Q -exciton roughly 19 ± 2 meV below X . The optical sidebands coincide with a low intensity bump that fits the predicted energies. The direct spin-unlike exciton (D) should be 40 meV to the red of X , but cannot be resolved clearly, possibly because R_1 is broad and intense enough to merge with the weak PL of D . Its momentum-indirect counterpart in K' should have the same energy, thus we can estimate its phonon sidebands, which fit the strong R_2 peak and the corresponding low-intensity feature to the red.

Assuming the nature of the phonon sidebands does not change fundamentally in a charged environment it is worth a try to treat the charged spectrum in a similar fashion. Analogous to the trion, the energy of the peaks should redshift upon interaction with free charge carriers. When shifting the Q -valley by the trion binding energy, it fits the two most intense replica peaks in the charged spectrum (R_1^-, R_2^-). However, R_2^- also matches D shifted by the trion binding energy. This could explain the relatively strong signal at this energy. The weak feature to the red could then charged acoustic replica of K' .

4.3.2 REFLECTION SPECTRUM

The reflection spectrum can be seen in figure 4.4. The neutral spectrum shows a clear signature of the main exciton resonance (X). This spectral feature in an hBN encapsulated sample has the shape of a fano resonance, because of interference effects, caused by the encapsulation. The TMD-hBN heterostructure acts as a microcavity and shows very high reflectivity at the resonance frequency[43]. Upon tuning the gate to negative voltages, the absorption and reflection at the exciton resonance is suppressed and the trion resonance forms (X^-). Just like in PL this resonance exhibits a splitting due to coulomb exchange energy.

4.4 MEASURING THE VALLEY ZEEMAN EFFECT

As described in section 2.4 the band gap and exciton energies in TMDS shift when exposed to an out-of-plane magnetic field. These shifts are reversed in light of opposite helicity and differ

for different types of excitonic processes. Measuring the splitting, and quantifying it through the g -factor can yield a deeper insight in the nature of the spectral features. Figure 4.5 and 4.6 show the PL and reflection spectra for different gate voltages at 0 and 8 T. Because of different magnetic shifts of the different peaks, looking at σ^+ and σ^- polarized spectra at high magnetic field can help to resolve features, that are otherwise hidden by inhomogeneous broadening. The first interesting feature to study in this fashion is the two trion peaks (X^-). At 8 T they reveal significant change in their splitting, merging to one peak in σ^+ while showing a clear splitting in σ^- . The trion fine structure as the result of electron-electron exchange interaction could yield an explanation for this difference. The singlet-state consists of an exciton and an electron of opposite spin at the K -point while the triplet state involves an additional electron in the K' -valley, but with the same spin component as the electron in the tightly bound exciton. Because these valleys shift in opposite directions, a different overall shift makes sense. This allows to also observe the different behavior with regards to the charge density. At high negative gate voltages, both peaks are less intense with the blue peak losing signal much more rapidly. The reasons for that are speculative at best. Recent measurements in ws_2 point to the singlet state being stable only at low temperatures[47]. Similarly, the triplet state in wse_2 could be more sensitive to large densities of free charge carriers.

4.4.1 G-FACTORS

The magnetic splitting ΔE can be quantified by the g -factor. Because ΔE is linear in magnetic field strength B , the peak positions can be fitted using simple linear regression where the slope is connected to the g -factor in the following fashion:

$$g = \frac{1}{\mu_B} \underbrace{\frac{\Delta E}{\Delta B}}_{slope} \quad (4.6)$$

Because the splitting is a lot smaller than the linewidth – 0.25 meV / T at a linewidth of 7 meV – the peaks have to be fitted using the procedures described in 4.2 to obtain a low error and therefore an accurate estimate for the g -factor. Not all features can be resolved well enough, because of either a bad signal to noise ratio or linewidth-related blending with other peaks. The shifts and calculated g -factors can be seen in figures 4.7 and 4.8.

EXITON & TRION

PHONON SIDEBANDS

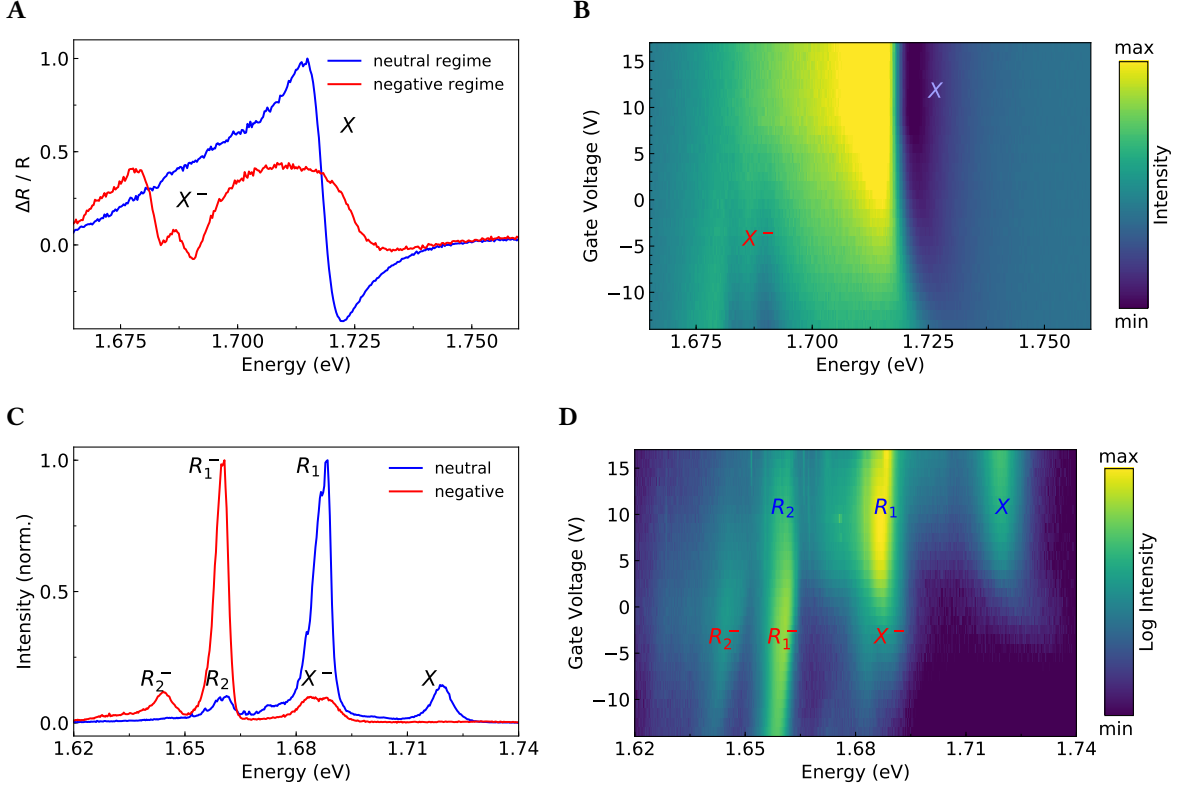


Figure 4.4: Reflection of wse₂ at different doping levels. **A** The reflection spectrum of wse₂ in a neutral and negatively charged regime. The neutral spectrum shows a strong response, corresponding to the main exciton resonance (X). The absorption of the exciton almost vanishes in the charged spectrum and a double dip appears, that corresponds to the trion resonance, resolving the typical exchange splitting (X⁻). **B** Reflection spectra at different voltages. The exciton absorption shows a similar response as in PL, however stretched to lower voltages. The absorption at the trion resonance can be resolved much better, than the corresponding peaks in PL. Photoluminescence of wse₂ at different doping levels. **C** Spectra in the neutral and negatively charged regime. The PL of the exciton (X) is clearly visible at the blue end of the spectrum. The replica peaks (R_1 , R_2) correspond to acoustic phonon sidebands of Q - and K' -indirect excitons with low-intensity features to the red indicating optical sidebands. In a negatively charged regime, they vanish in favor of redshifted peaks, that correspond to the trion (X⁻) that is split by electron-electron exchange interaction, and its momentum indirect counterparts. While R_1^- fits the picture as an acoustic sideband of X⁻, R_2^- seems to be the charged spin-unlike dark state. **D** Spectral features in a gate-sweep. The plot can be divided into a neutral and charged regime below and above 5V. This threshold is a signature of unintentional n-doping and varies across the sample.

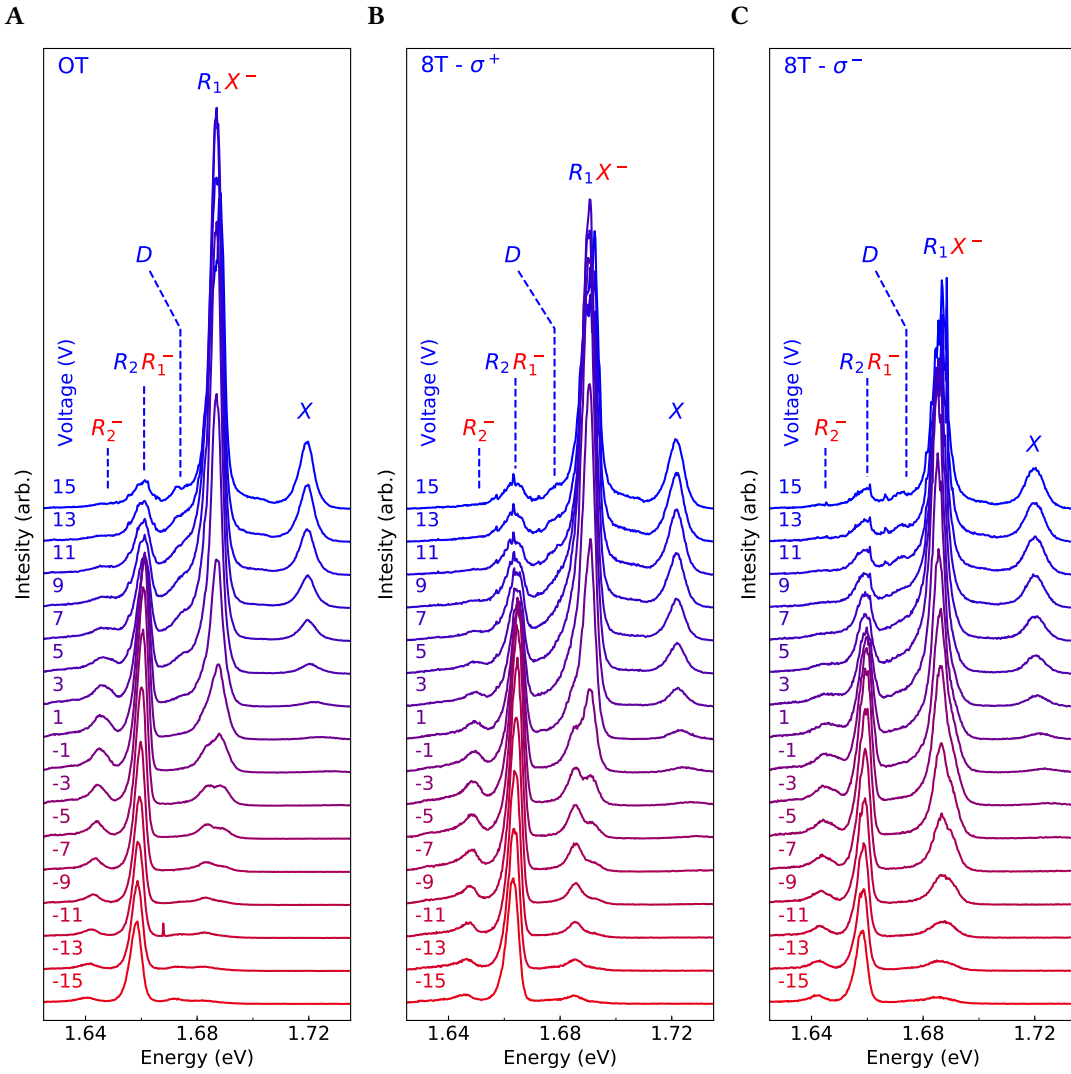


Figure 4.5: PL spectra of ws_2 at high magnetic fields for different gate voltages. In the neutral spectrum the dark exciton (D) lies too close to the strong phonon sideband R_1 to be resolved clearly. The strong splitting of this feature reveals D more clearly in the σ^+ -polarized spectrum at 8T (gfactor). The trion peak in the negative regime is composed of at least two features. As can be seen these peaks have different g-factors as well, that lead to a wide split in σ^+ and merge to one feature in σ^- .

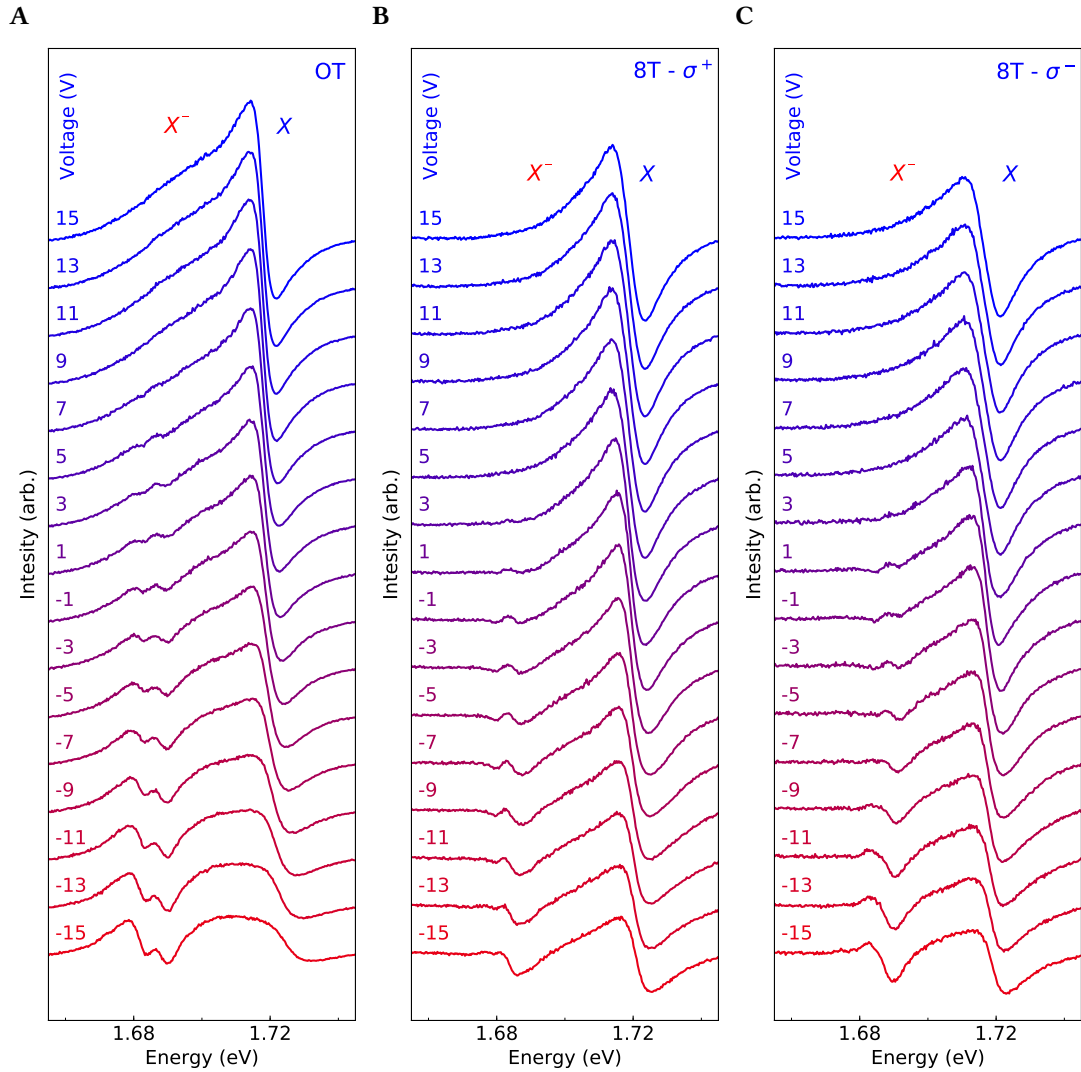


Figure 4.6: PL spectra of wse₂ at high magnetic fields for different gate voltages. In the neutral spectrum, towards the positive end, the replica peaks R_1 and R_2 get significantly skewed at 8 T, pointing towards several underlying peaks with different g -factors. The trion peak in the negative regime is composed of at least two features. As can be seen these peaks have different g -factors as well, that lead to a wide split in σ^+ and merge to one feature in σ^- .

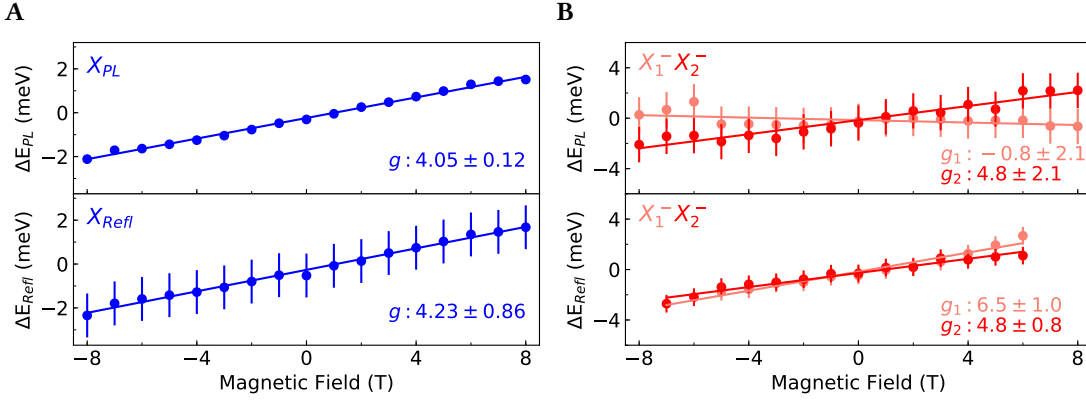


Figure 4.7: Exciton valley splitting in PL and reflection. **A** The g -factor of the neutral exciton is in good agreement with theory and previous studies. The fit of the reflection measurement has a large error bar, because of the complicated lineshape. Since the variance of the data points is low, this seems to be a systematic error. **B** The trion peak can only be reliably modeled in the reflection spectrum because of insufficient signal-to-noise ratio and limitations of the linewidth. The fits suggest a different g -factor for the two subfeatures.

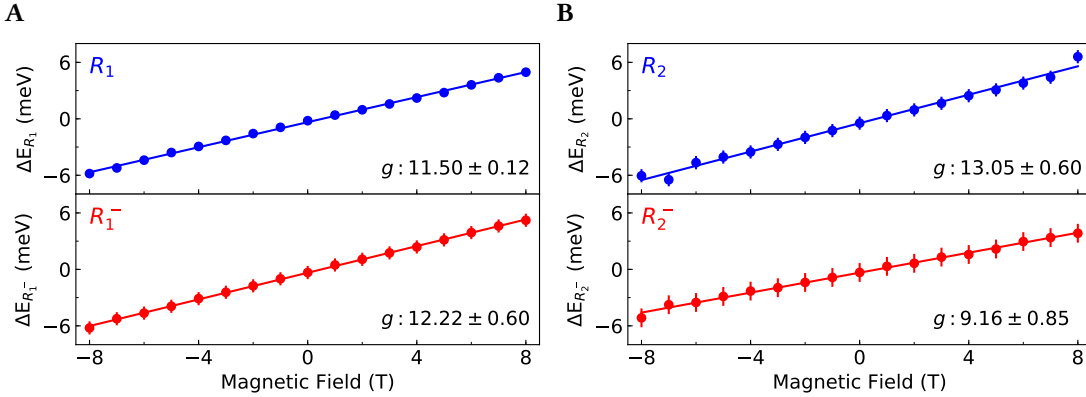


Figure 4.8: Valley splitting of phonon replica. **A** The intense R_1 peak and its charged counterpart R_1^- show a similar g -factor, suggesting the same origin. This is consistent with the proposed model, that identifies the peaks as acoustic sidebands of momentum-indirect excitons in the Q -valley. R_1 is of particular interest, because this feature conventionally is attributed to the trion. The strong difference in the g -factor however suggests a different origin than the trion feature, even though they share the same energy in the spectrum. **B** The neutral peak R_2 was previously identified as a phonon sideband of the K' -indirect exciton. The high g -factor however does not offer an argument to support . However, the charged counterpart R_2^- has a similar g -factor as was previously measured for D , which underscores the assumption of the feature being the charged spin-unlike exciton in K .

BIBLIOGRAPHY

- ¹F. Langer, C. P. Schmid, S. Schlauderer, M. Gmitra, J. Fabian, P. Nagler, C. Schüller, T. Korn, P. G. Hawkins, J. T. Steiner, U. Hettner, S. W. Koch, M. Kira, and R. Huber, “Lightwave valleytronics in a monolayer of tungsten diselenide”, *Nature* **557**, 76–80 (2018).
- ²Q. H. Wang, K. Kalantar-Zadeh, A. Kis, J. N. Coleman, and M. S. Strano, “Electronics and optoelectronics of two-dimensional transition metal dichalcogenides”, *Nature Nanotechnology* **7**, 699–712 (2012).
- ³D. Xiao, G.-B. Liu, W. Feng, X. Xu, and W. Yao, “Coupled spin and valley physics in monolayers of MoS₂ and other group-VI dichalcogenides”, *Physical Review Letters* **108** (2012) 10.1103/PhysRevLett.108.196802.
- ⁴A. Chernikov, T. C. Berkelbach, H. M. Hill, A. Rigosi, Y. Li, O. B. Aslan, D. R. Reichman, M. S. Hybertsen, and T. F. Heinz, “Exciton binding energy and nonhydrogenic rydberg series in monolayer WS₂”, *Physical Review Letters* **113** (2014) 10.1103/PhysRevLett.113.076802.
- ⁵A. V. Stier, N. P. Wilson, G. Clark, X. Xu, and S. A. Crooker, “Probing the influence of dielectric environment on excitons in monolayer WSe₂: insight from high magnetic fields”, *Nano Letters* **16**, 7054–7060 (2016).
- ⁶S. Borghardt, J.-S. Tu, F. Winkler, J. Schubert, W. Zander, K. Leosson, and B. E. Kardynał, “Engineering of optical and electronic band gaps in transition metal dichalcogenide monolayers through external dielectric screening”, *Physical Review Materials* **1** (2017) 10.1103/PhysRevMaterials.1.054001.
- ⁷T. Jakubczyk, K. Nogajewski, M. R. Molas, M. Bartos, W. Langbein, M. Potemski, and J. Kasprzak, “Impact of environment on dynamics of exciton complexes in a WS₂ monolayer”, *2D Materials* **5**, 031007 (2018).
- ⁸A. Neumann, J. Lindlau, L. Colombier, M. Nutz, S. Najmaei, J. Lou, A. D. Mohite, H. Yamaguchi, and A. Högele, “Opto-valleytronic imaging of atomically thin semiconductors”, *Nature Nanotechnology* **12**, 329–334 (2017).
- ⁹N. Zibouche, A. Kuc, J. Musfeldt, and T. Heine, “Transition-metal dichalcogenides for spintronic applications: spintronics beyond graphene”, *Annalen der Physik* **526**, 395–401 (2014).
- ¹⁰J. P. Echeverry, B. Urbaszek, T. Amand, X. Marie, and I. C. Gerber, “Splitting between bright and dark excitons in transition metal dichalcogenide monolayers”, *Physical Review B* **93** (2016) 10.1103/PhysRevB.93.121107.
- ¹¹C. Robert, T. Amand, F. Cadiz, D. Lagarde, E. Courtade, M. Manca, T. Taniguchi, K. Watanabe, B. Urbaszek, and X. Marie, “Fine structure and lifetime of dark excitons in transition metal dichalcogenide monolayers”, *Physical Review B* **96** (2017) 10.1103/PhysRevB.96.155423.

BIBLIOGRAPHY

- ¹²G. Wang, C. Robert, M. M. Glazov, F. Cadiz, E. Courtade, T. Amand, D. Lagarde, T. Taniguchi, K. Watanabe, B. Urbaszek, and X. Marie, “In-plane propagation of light in transition metal dichalcogenide monolayers: optical selection rules”, *Physical Review Letters* **119** (2017) 10 . 1103/PhysRevLett.119.047401.
- ¹³E. Courtade, M. Semina, M. Manca, M. M. Glazov, C. Robert, F. Cadiz, G. Wang, T. Taniguchi, K. Watanabe, M. Pierre, W. Escoffier, E. L. Ivchenko, P. Renucci, X. Marie, T. Amand, and B. Urbaszek, “Charged excitons in monolayer WSe₂: experiment and theory”, *Physical Review B* **96** (2017) 10 . 1103/PhysRevB.96.085302.
- ¹⁴M. Sidler, P. Back, O. Cotlet, A. Srivastava, T. Fink, M. Kroner, E. Demler, and A. Imamoglu, “Fermi polaron-polaritons in charge-tunable atomically thin semiconductors”, *Nature Physics* **13**, 255–261 (2016).
- ¹⁵D. K. Efimkin and A. H. MacDonald, “Many-body theory of trion absorption features in two-dimensional semiconductors”, *Physical Review B* **95** (2017) 10 . 1103/PhysRevB.95.035417.
- ¹⁶R. Schmidt, T. Enss, V. Pietilä, and E. Demler, “Fermi polarons in two dimensions”, *Physical Review A* **85** (2012) 10 . 1103/PhysRevA.85.021602.
- ¹⁷T. Kato and T. Kaneko, “Optical detection of a highly localized impurity state in monolayer tungsten disulfide”, *ACS Nano* **8**, 12777–12785 (2014).
- ¹⁸S. Zhang, C.-G. Wang, M.-Y. Li, D. Huang, L.-J. Li, W. Ji, and S. Wu, “Defect structure of localized excitons in a WSe₂ monolayer”, *Physical Review Letters* **119** (2017) 10 . 1103 / PhysRevLett.119.046101.
- ¹⁹J. Lindlau, C. Robert, V. Funk, J. Förste, M. Förg, L. Colombier, A. Neumann, E. Courtade, S. Shree, T. Taniguchi, K. Watanabe, M. M. Glazov, X. Marie, B. Urbaszek, and A. Högele, “Identifying optical signatures of momentum-dark excitons in transition metal dichalcogenide monolayers”, arXiv:1710.00988 [cond-mat] (2017).
- ²⁰C. Zhang, Y. Chen, A. Johnson, M.-Y. Li, L.-J. Li, P. C. Mende, R. M. Feenstra, and C.-K. Shih, “Probing critical point energies of transition metal dichalcogenides: surprising indirect gap of single layer WSe₂”, *Nano Letters* **15**, 6494–6500 (2015).
- ²¹W.-T. Hsu, L.-S. Lu, D. Wang, J.-K. Huang, M.-Y. Li, T.-R. Chang, Y.-C. Chou, Z.-Y. Juang, H.-T. Jeng, L.-J. Li, and W.-H. Chang, “Evidence of indirect gap in monolayer WSe₂”, *Nature Communications* **8** (2017) 10 . 1038/s41467-017-01012-6.
- ²²Z. Jin, X. Li, J. T. Mullen, and K. W. Kim, “Intrinsic transport properties of electrons and holes in monolayer transition-metal dichalcogenides”, *Physical Review B* **90** (2014) 10 . 1103 / PhysRevB.90.045422.
- ²³M. Van der Donck, M. Zarenia, and F. M. Peeters, “Excitons, trions, and biexcitons in transition-metal dichalcogenides: magnetic-field dependence”, *Physical Review B* **97** (2018) 10 . 1103 / PhysRevB.97.195408.
- ²⁴A. Srivastava, M. Sidler, A. V. Allain, D. S. Lembke, A. Kis, and A. Imamoğlu, “Valley zeeman effect in elementary optical excitations of monolayer WSe₂”, *Nature Physics* **11**, 141–147 (2015).

BIBLIOGRAPHY

- ²⁵D. V. Rybkovskiy, I. C. Gerber, and M. V. Durnev, “Atomically inspired $k \cdot p$ approach and valley zeeman effect in transition metal dichalcogenide monolayers”, *Physical Review B* **95** (2017) 10.1103/PhysRevB.95.155406.
- ²⁶J. Chen, W. Tang, B. Tian, B. Liu, X. Zhao, Y. Liu, T. Ren, W. Liu, D. Geng, H. Y. Jeong, H. S. Shin, W. Zhou, and K. P. Loh, “Chemical vapor deposition of high-quality large-sized MoS₂ crystals on silicon dioxide substrates”, *Advanced Science* **3**, 1500033 (2016).
- ²⁷A. K. Geim and K. S. Novoselov, “The rise of graphene”, *Nature Materials* **6**, 183–191 (2007).
- ²⁸V. Funk, “Spectroscopy of momentum-dark excitons in layered semiconductors” (LMU München, 2017).
- ²⁹W. Zhao, Z. Ghorannevis, K. K. Amara, J. R. Pang, M. Toh, X. Zhang, C. Kloc, P. H. Tan, and G. Eda, “Lattice dynamics in mono- and few-layer sheets of WS₂ and WSe₂”, *Nanoscale* **5**, 9677 (2013).
- ³⁰X. Zhang, X.-F. Qiao, W. Shi, J.-B. Wu, D.-S. Jiang, and P.-H. Tan, “Phonon and raman scattering of two-dimensional transition metal dichalcogenides from monolayer, multilayer to bulk material”, *Chemical Society Reviews* **44**, 2757–2785 (2015).
- ³¹P. Tonndorf, R. Schmidt, P. Böttger, X. Zhang, J. Börner, A. Liebig, M. Albrecht, C. Kloc, O. Gordan, D. R. T. Zahn, S. Michaelis de Vasconcellos, and R. Bratschitsch, “Photoluminescence emission and raman response of monolayer MoS₂, MoSe₂, and WSe₂”, *Optics Express* **21**, 4908 (2013).
- ³²E. Courtade, B. Han, S. Nakhaie, C. Robert, X. Marie, P. Renucci, T. Taniguchi, K. Watanabe, L. Geelhaar, J. M. J. Lopes, and B. Urbaszek, “Spectrally narrow exciton luminescence from monolayer MoS₂ exfoliated onto epitaxially grown hexagonal BN”, arXiv:1804.06623 [cond-mat] (2018).
- ³³B. Arnaud, S. Lebègue, P. Rabiller, and M. Alouani, “Huge excitonic effects in layered hexagonal boron nitride”, *Physical Review Letters* **96** (2006) 10.1103/PhysRevLett.96.026402.
- ³⁴H. Li, J. Wu, X. Huang, Z. Yin, J. Liu, and H. Zhang, “A universal, rapid method for clean transfer of nanostructures onto various substrates”, *ACS Nano* **8**, 6563–6570 (2014).
- ³⁵A. Castellanos-Gomez, M. Buscema, R. Molenaar, V. Singh, L. Janssen, H. S. J. v. d. Zant, and G. A. Steele, “Deterministic transfer of two-dimensional materials by all-dry viscoelastic stamping”, *2D Materials* **1**, 011002 (2014).
- ³⁶F. Pizzocchero, L. Gammelgaard, B. S. Jessen, J. M. Caridad, L. Wang, J. Hone, P. Bøggild, and T. J. Booth, “The hot pick-up technique for batch assembly of van der waals heterostructures”, *Nature Communications* **7**, 11894 (2016).
- ³⁷D. H. Tien, J.-Y. Park, K. B. Kim, N. Lee, T. Choi, P. Kim, T. Taniguchi, K. Watanabe, and Y. Seo, “Study of graphene-based 2d-heterostructure device fabricated by all-dry transfer process”, *ACS Applied Materials & Interfaces* **8**, 3072–3078 (2016).
- ³⁸K.-H. Jung, D. G. Kim, and S.-B. Jung, “Adhesion of PDMS substrates assisted by plasma graft polymerization”, *Surface and Interface Analysis* **48**, 597–600 (2016).
- ³⁹Y.-C. Lin, C.-C. Lu, C.-H. Yeh, C. Jin, K. Suenaga, and P.-W. Chiu, “Graphene annealing: how clean can it be?”, *Nano Letters* **12**, 414–419 (2012).

BIBLIOGRAPHY

- ⁴⁰N. Klein and H. Gafni, “The maximum dielectric strength of thin silicon oxide films”, IEEE Transactions on Electron Devices **ED-13**, 281–289 (1966).
- ⁴¹A. L. Stancik and E. B. Brauns, “A simple asymmetric lineshape for fitting infrared absorption spectra”, Vibrational Spectroscopy **47**, 66–69 (2008).
- ⁴²U. Fano, “Effects of configuration interaction on intensities and phase shifts”, Physical Review **124**, 1866–1878 (1961).
- ⁴³G. Suri, Y. Zhou, A. A. High, D. S. Wild, C. Shu, K. De Greve, L. A. Jauregui, T. Taniguchi, K. Watanabe, P. Kim, M. D. Lukin, and H. Park, “Large excitonic reflectivity of monolayer MoSe₂ encapsulated in hexagonal boron nitride”, Physical Review Letters **120** (2018) 10 . 1103 / PhysRevLett.120.037402.
- ⁴⁴G. Moody, C. Kavir Dass, K. Hao, C.-H. Chen, L.-J. Li, A. Singh, K. Tran, G. Clark, X. Xu, G. Berghäuser, E. Malic, A. Knorr, and X. Li, “Intrinsic homogeneous linewidth and broadening mechanisms of excitons in monolayer transition metal dichalcogenides”, Nature Communications **6** (2015) 10 . 1038/ncomms9315.
- ⁴⁵O. A. Ajayi, J. V. Ardelean, G. D. Shepard, J. Wang, A. Antony, T. Taniguchi, K. Watanabe, T. F. Heinz, S. Strauf, X.-Y. Zhu, and J. C. Hone, “Approaching the intrinsic photoluminescence linewidth in transition metal dichalcogenide monolayers”, 2D Materials **4**, 031011 (2017).
- ⁴⁶C. R. Zhu, G. Wang, B. L. Liu, X. Marie, X. F. Qiao, X. Zhang, X. X. Wu, H. Fan, P. H. Tan, T. Amand, and B. Urbaszek, “Strain tuning of optical emission energy and polarization in monolayer and bilayer MoS₂”, Physical Review B **88** (2013) 10 . 1103 / PhysRevB.88.121301.
- ⁴⁷D. Vaclavkova, J. Wyzula, K. Nogajewski, M. Bartos, A. O. Slobodeniuk, C. Faugeras, M. Potemski, and M. R. Molas, “Singlet and triplet trions in WS₂ monolayer encapsulated in hexagonal boron nitride”, arXiv:1802.05538 [cond-mat] (2018).